SCIENCE CHINA
Chemistry

•ARTICLES•

February 2022 Vol.65 No.2: 339–352
https://doi.org/10.1007/s11426-021-1113-0

Visualizing Aβ deposits in live young AD model mice with a simple red/near-infrared-fluorescent AIEgen

Yipu Wang[1†], Dong Mei[2†], Xinyi Zhang[1], Da-Hui Qu[1] & Ju Mei[1*]

[1]*Key Laboratory for Advanced Materials, Feringa Nobel Prize Scientist Joint Research Center, Frontiers Science Center for Materiobiology and Dynamic Chemistry, Joint International Research Laboratory for Precision Chemistry and Molecular Engineering, Institute of Fine Chemicals, School of Chemistry & Molecular Engineering, East China University of Science & Technology, Shanghai 200237, China;*
[2]*Clinical Research Center, Beijing Children's Hospital, Capital Medical University, National Center for Children's Health, Beijing 100045, China*

Received August 11, 2021; accepted September 3, 2021; published online November 8, 2021

Precise and early detection of β-amyloid (Aβ) deposits *in situ* and in real time is pivotal to the diagnosis and early intervention of Alzheimer's disease (AD). Optical imaging stands out to be a promising technique for such a task; however, it still remains a big challenge, due to the lack of high-performance imaging contrast agent. Restricted by poor blood-brain barrier (BBB) penetrability, short-wavelength excitation and emission, as well as the aggregation-caused quenching effect, the widely used gold-standard probes cannot be used for early *in-vivo* imaging of Aβ deposits. Herein, we integrate the Aβ deposits-favored geometry, amphiphilic and zwitterionic molecular structure, extended D-π-A electronic structure, and 3D conformation into one molecule, facilely establishing a simple and economic imaging contrast agent that enjoys high specificity and affinity to Aβ deposits, good BBB penetrability, bright red/near-infrared fluorescence, low interference from autofluorescence, aggregation-induced emission (AIE) feature, high signal-to-noise ratio (SNR), and high contrast. *In-vitro*, *ex-vivo*, and *in-vivo* experiments with different strains of mice indicate that AIE-CNPy-AD holds the universality to Aβ deposits identification. Noteworthily, AIE-CNPy-AD is even able to precisely trace the small and sparsely-distributed Aβ deposits in AD model mice as young as 4-month-old APP/PS1 mice, the youngest having Aβ deposits. Moreover, the present probe could clearly reveal the increase and enlargement of Aβ deposits as the mice grow. Therefore, AIE-CNPy-AD might be an ideal alternative for early AD diagnosis and highly reliable monitoring of AD progression.

Aβ deposits, AIE, Alzheimer's disease (AD), red/NIR fluorescence, *in-vivo* imaging, diagnosis

Citation: Wang Y, Mei D, Zhang X, Qu DH, Mei J. Visualizing Aβ deposits in live young AD model mice with a simple red/near-infrared-fluorescent AIEgen. *Sci China Chem*, 2022, 65: 339–352, https://doi.org/10.1007/s11426-021-1113-0

1 Introduction

Alzheimer's disease (AD) is a degenerative disease of the nervous system, which will lead to memory loss, behaviour disorder, cognitive decline, and eventually death [1]. According to the statistics, there are about 50 million patients with Alzheimer's disease all over the world. It is predicted that the number of AD patients will increase to 150 million by 2050, exerting serious social and economic burden on countries worldwide [1]. Currently, clinical diagnosis of AD patients is mainly through the combination of the inquiring of the patients' genetic history, neuropsychiatric test, neuropathological diagnosis, and neuroimaging diagnosis. Only after death of AD patients, can final diagnosis be confirmed by brain tissue examination [1]. β-Amyloid (Aβ) hypothesis has shown that the extracellular accumulation of β-amyloid peptides forming fibrotic deposits is one of the neuropatho-

†These authors contributed equally to this work.
*Corresponding author (email: daisymeiju@ecust.edu.cn)

logical hallmarks of AD [1,2], as such early detection of Aβ deposits *in vivo* with low damage plays extremely important role in the diagnosis and subsequent intervention and prevention of AD [3–10].

By far, a large number of imaging techniques, such as magnetic resonance imaging (MRI), positron emission tomography (PET), and single photon emission computed tomography (SPECT), have been utilized to clinically diagnose AD [9,10]. Nevertheless, MRI can only image large deposits because of its limited sensitivity; PET needs radioisotopes which are hard to be obtained and probably impose radioactive exposure danger on patients; and SPECT has relatively higher background noise and the tracers used in this technique usually have poor BBB penetrating ability. Drawbacks of these techniques hamper their wide application in early diagnosis of AD. Compared with the above techniques, fluorescence imaging technique enjoys real-time and *in-situ* monitoring ability, high sensitivity, low biological toxicity, non-invasiveness, superior spatiotemporal resolution, low cost, and technical simplicity, making it promising in the imaging of Aβ deposits and diagnosis of AD [7,8,11–30].

Thioflavin T (ThT) and thioflavin S (ThS) are the most commonly used fluorescent dyes to histologically stain Aβ deposits [7,8,11]. However, the excessively excellent water-solubility of these dyes limits their ability to penetrate the BBB [15], rendering them merely effective in *in-vitro* and *ex-vivo* imaging of Aβ deposits. Moreover, ThT is hardly able to distinguish Aβ peptides of different aggregation levels [12]. The short-wavelength excitation and emission of probes like ThT and ThS prevent them to be used for *in-vivo* imaging, because of the unsatisfactory deep-tissue penetration ability and non-negligible photodamage to organisms. In addition, these fluorophores suffer from aggregation-caused quenching (ACQ) effect that results in self-quenching of FL signal after binding to Aβ species, and the reduced detection sensitivity and imaging resolution [7,8,12]. Sensitive and reliable probes with high ability to penetrate BBB and deep tissues which can be employed to detect and image Aβ deposits *in vivo* are urgently desirable [7,8].

By analysing the structure and performance of the small molecular fluorescent probes reported for Aβ deposits detection, it can be found that the fluorescent probes having rod-like geometric configurations and donor-acceptor (D-A) electronic structures usually perform relatively well (Figure 1a) [7,8,13–26]. On the one hand, the rod-like structured probes have a certain similarity with Aβ deposits in morphology, which is conducive to the binding of probes and Aβ deposits and subsequently benefits the specificity. On the other hand, the probes with D-A effect are sensitive to the environmental hydrophobicity, with the emissions intensified when bound to hydrophobic areas of amyloids abundant in β-sheet structures. Though these two essential structural features can guarantee the basic performance of the probes, other deficiencies still seriously affect the detection and imaging performance of these probes. Most of the reported probes show ACQ effect [7,8,13], resulting in relatively high background and insufficient SNR. Moreover, simple D-A structures in probes like ThT cannot ensure red or near-infrared (NIR) emission, which can neither avoid the interference from auto-fluorescence of organisms nor assure the ability to penetrate deep tissues.

Based on the analysis above, we sort out four main elements which should be satisfied to realize high-performance fluorescent probes for detecting and imaging Aβ deposits *in vivo* at an early stage (Figure 1b): (1) geometric configurations matching the β-sheet structure; (2) balanced hydrophilicity and hydrophobicity which guarantees the BBB crossing ability and high SNR; (3) strong D-A effect ensuring fluorescent response, long-wavelength excitation and emission, and large Stokes shift; (4) anti-ACQ effect that enhances the fluorescent response, SNR, and imaging resolution. Accordingly, the rod-like geometric configuration that favors the binding to Aβ deposits, hydrophilic unit-decorated hydrophobic skeleton ensuring high affinity to Aβ deposits and good BBB penetrability, large D-π-A electronic structure guaranteeing red/NIR fluorescence and low interference from autofluorescence, and 3D conformation assuring aggregation-induced emission (AIE) effect, high SNR and contrast are ingeniously integrated into one molecule to meet the above four requirements (Figure 1b).

As a proof of concept, AIE-CNPy-AD is designed following the “multi-pronged” strategy. In this molecule, electron-donating dimethylamino, electron-accepting acetonitrile and pyridyl group are linked together *via* single bonds and bridged by benzyl groups and a C=C double bond, affording a large 3D rod-like configured D-π-A framework. Benefited from such a skeleton, strong Aβ deposit-binding capability, efficient AIE effect [31] and bright red/NIR fluorescence are achieved. Furthermore, the hydrophilic propanesulfonate group is attached to the hydrophobic molecular backbone to generate the zwitterionic and amphiphilic AIE-CNPy-AD, endowing AIE-CNPy-AD with low background, high SNR and good BBB penetrating ability. Since as compared with traditional ACQ probes, AIE probes often have the advantages of good photo-stability, high SNR, and high-resolution and resistance to photo-bleaching, the imaging performance of these fluorescent probes is greatly improved [32–39]. As a result, the rod-like amphiphilic red/NIR-emissive AIE probe AIE-CNPy-AD possesses high specificity to Aβ deposits, deep-tissue penetrating ability, good resistance to auto-fluorescence interference from organisms, good photo-stability, and high-contrast imaging ability.

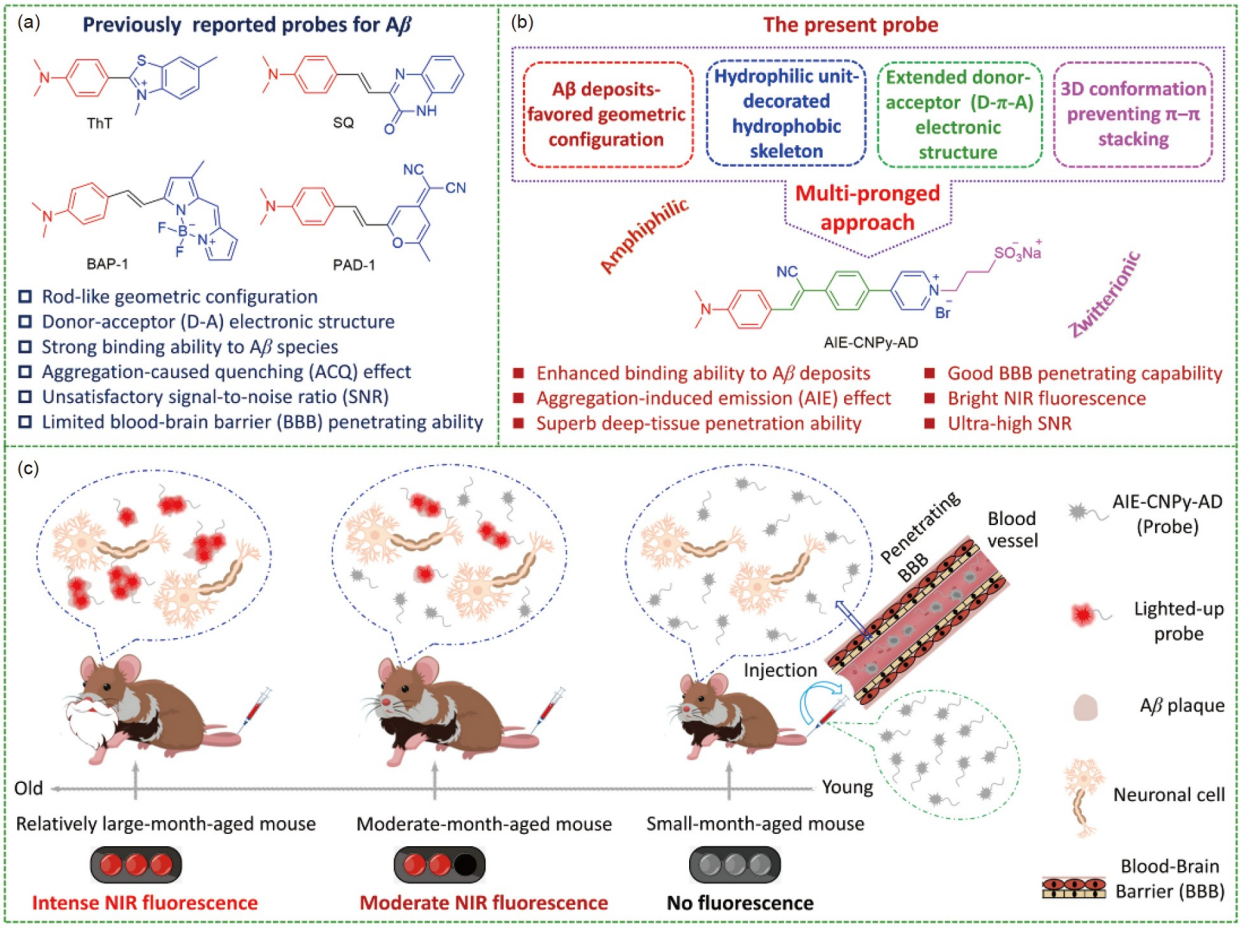

Figure 1 The "multi-pronged" design principle. (a) Representatives of typical probes for Aβ detection with rod-like configuration and D-A electron structure; (b) our red/NIR AIE probe (AIE-CNPy-AD) for Aβ deposits rationally constructed based on the proposed "multi-pronged" design strategy; (c) schematic illustration of the *in-vivo* imaging of Aβ deposits with AIE-CNPy-AD in brains of AD model mice in different age periods *via* tail vein injection, and the potential of AIE-CNPy-AD in early diagnosis of AD (color online).

With the aid of the above merits, the elaborated probe AIE-CNPy-AD is able to realize detection of Aβ fibrils *in vitro* with high SNR and *in-situ* mapping of Aβ deposits *in vivo* with high sensitivity, and high fidelity and contrast. More importantly, the precise *in-situ* and *in-vivo* mapping ability of Aβ deposits is not limited by mouse strains. It is worth mentioning that even small and sparsely distributed Aβ deposits in the brains of AD transgenic mice APP/PS1 as young as 4-month old could be visualized by our probe. It is reported that the Aβ deposits would not appear when the APP/PS1 mice are younger than 4-month old. Moreover, the increase and enlargement of Aβ deposits as well as the progression of AD as the mice grow could be clearly revealed by the present probe. In other words, AIE-CNPy-AD is very promising in early diagnosis and highly reliable monitoring of AD progression (Figure 1c). Besides, we clearly put forward the "multi-pronged" strategy to rationally design AIE-active red/NIR imaging contrast agent for light-up and *in-situ* tracing of Aβ deposits in mice of different strains and ages.

2 Experimental

2.1 Materials and instruments

Common reagents and raw materials were purchased from formal channels and analytically pure, and used without further purification. Aβ_{1-42} peptides were purchased from GL Biochem (Shanghai) Co., Ltd. Hen egg white lysozyme (HEWL) was purchased from Aladdin. Cell culture medium RPMI-1640, penicillin-streptomycin, and 0.25% trypsin were obtained from M&C Gene Technology (Beijing, China). Fetal bovine serum was purchased from Gemini Bio-Products (Calabasas, California, USA). All other solvents and reagents for biological experiments were of analytical grade.

The molecular structures were characterized using ^{1}H nuclear magnetic resonance (^{1}H NMR), ^{13}C NMR and high-resolution mass spectroscopy (HRMS). ^{1}H NMR and ^{13}C NMR spectra were recorded on a Brüker AV-400 spectrometer (Germany) by using deuterated solvents with 0.03% tetramethylsilane (TMS) as internal standard. The HRMS spectra were taken on an HP 5958 mass spectrometer (Agi-

lent, USA) with the electronic spray ionization mode. The ultraviolet-visible (UV-Vis) absorption spectra were recorded in 1 cm slit quartz cells on an Agilent Cary 60 UV-Vis spectrometer (USA). The photoluminescence spectra were recorded in 1 cm or 4 mm-slit quartz cells on an Agilent Cary Eclipse Fluorescence spectrophotometer (USA). Photographs were taken with a Canon EOS 6D digital camera (Japan). Buffer solutions were prepared with Mettler Toledo FE28-Bio (Switzerland). Aβ_{1-42} fibril samples were prepared by sonication in a SB-800DT water-bath sonicator and vortexed by digital Vortex-Genie® 2 mixer. Transmission electron microscopy (TEM) images were obtained on a JEM-1400 biological transmission electron microscope. Fluorescent images of brain slices were obtained by a confocal laser scanning microscope (CLSM, Nikon, Japan). The live mice were imaged with a LivingImage system and the relative fluorescence intensity was analyzed by LivingImage 4.3.1 software (Caliper).

2.2 Synthesis of AIE-CNPy-AD

(*Z*)-3-(4-(dimethylamino)phenyl)-2-(4-(pyridin-4-yl)phenyl)acrylonitrile (PyDPACN-N) is synthesized according to the literature [39]. The **1** (294 mg, 1.500 mmol), **2** (268 mg, 1.800 mmol), sodium hydroxide (72 mg, 1.800 mmol) and EtOH (20 mL) were added into a 100 mL two-necked round-bottomed flask. The flask was flushed with dry nitrogen for three times. Then the mixture was stirred overnight at room temperature. Yellow solids were filtered out and washed thoroughly with EtOH to generate **3** (Figure S1, Supporting Information online), yield: 85.4%. ^{1}H NMR (400 MHz, $CDCl_3$) δ 7.85 (d, J = 9.0 Hz, 2H), 7.55−7.46 (m, 4H), 7.38 (s, 1H), 6.72 (d, J = 9.0 Hz, 2H), 3.07 (s, 6H).

The **3** (98 mg, 0.300 mmol), **4** (44 mg, 0.360 mmol), $Pd(PPh_3)_4$ (17 mg, 0.015 mmol), 2 M K_2CO_3 solution (2 mL) and tetrahydrofuran (THF, 10 mL) were added into a 100 mL two-necked round-bottomed flask. The flask was flushed with dry nitrogen for three times. Then the mixture was heated to 85 °C for 12 h. After the termination of the reaction, the resultant mixture was extracted with dichloromethane (DCM) for three times, and the collected organic layers were concentrated by a rotatory evaporator. Then the crude product was purified by column chromatography to obtain PyDPACN-N (Figure S1), yield: 73.2%. ^{1}H NMR (400 MHz, $CDCl_3$) δ 8.70 (d, J = 5.9 Hz, 2H), 7.90 (d, J = 8.9 Hz, 2H), 7.79 (d, J = 8.5 Hz, 2H), 7.72 (d, J = 8.5 Hz, 2H), 7.69 (d, J = 6.0 Hz, 2H), 7.51 (s, 1H), 6.74 (d, J = 9.0 Hz, 2H), 3.09 (s, 6H).

PyDPACN-N (164 mg, 0.500 mmol), sodium 3-bromopropanesulfonate (**5**, 225 mg, 2.000 mmol), and CH_3CN (20 mL) were added into a 100 mL two-necked round-bottomed flask. The flask was flushed with dry nitrogen three times. Then the mixture was refluxed for 96 h. Solids were filtered out from cooled mixture, and washed thoroughly with THF and water to afford the target product. AIE-CNPy-AD: Yield: 26.0%. ^{1}H NMR (400 MHz, DMSO-d_6) δ 9.11 (d, J = 7.0 Hz, 2H), 8.57 (d, J = 7.0 Hz, 2H), 8.21 (d, J = 8.7 Hz, 2H), 8.07 (s, 1H), 7.95 (t, J = 9.0 Hz, 4H), 6.86 (d, J = 9.1 Hz, 2H), 4.72 (t, J = 6.8 Hz, 2H), 3.05 (d, J = 5.5 Hz, 6H), 2.46 (t, J = 7.2 Hz, 2H), 2.31–2.22 (m, 2H). ^{13}C NMR (100 MHz, DMSO-d_6) δ 153.50, 152.12, 144.89, 144.61, 138.51, 132.34, 131.73, 128.82, 125.74, 124.09, 120.53, 119.01, 111.63, 100.58, 58.67, 46.95, 40.10, 39.90, 39.69, 39.48, 39.27, 39.06, 38.85, 27.26. HRMS (ESI-MS, m/z): $[M\text{-}Br]^+$ calcd. for $[C_{25}H_{25}N_3O_3SNa]^+$ 470.1514; found 470.1512.

2.3 Preparation of fibrillar HEWL

Lyophilized HEWL was dissolved at 14 mg/mL (1 mM) in sodium acetate-acetic acid buffer with 0.1 M NaCl (10 mM, pH = 3) [40]. The solution was incubated in an oil bath at 70 °C and magnetically stirred at 250 r/min for 12 h. The initially clear solution was observed to form cloudy aggregates by 1 h of incubation. The samples were stored at 4 °C before further use.

2.4 Preparation and characterization of Aβ_{1-42} fibrils

Aβ_{1-42} (0.25 mg) was dissolved in hexafluoroisopropanol (HFIP) and sonicated in a water-bath sonicator for 5 min at room temperature [41]. HFIP-treated solution was vortexed gently and incubated for 45 min at room temperature. After chilling solution on ice, the solvent was removed in a dry nitrogen stream. Dimethyl sulfoxide and PBS buffer (pH = 7.4) was added to the pretreated peptide film to afford a 0.2 mM solution, which was further incubated at 37 °C and shaken for 7 days to yield the desired samples of Aβ_{1-42} fibrils.

1 μL aged Aβ_{1-42} fibrils solution (0.2 mM) was added into water to dilute to a 10 μM solution. Samples for TEM measurement were prepared by depositing 10 μL of the appropriate solution onto a carbon-coated copper grid, keeping at room temperature for 20 min to ensure the adsorption of Aβ_{1-42} fibrils on the copper grid, and wicking the excess solution away with a small piece of filter paper. The samples were then stained with phosphotungstic acid. At last, the sample grids were allowed to be dried at room temperature and imaged on a JEM-1400 biological transmission electron microscope.

2.5 Cell lines for cytotoxicity assay

The human neuroblastoma cells (SH-SY5Y), mouse brain neuroblastoma cells (Neuro-2a), mouse breast cancer cells (4T1), and human breast cancer cells (MCF-7) were obtained

from the Institute of Basic Medical Science (Beijing, China). SH-SY5Y cells were cultured in DMEM/F-12 medium. Neuro-2a cells were cultured in DMEM with high glucose medium. 4T1 and MCF-7 cells were cultured in RPMI-1640 medium. All of the above media were supplemented with 10% fetal bovine serum and 1% (100 U/mL) penicillin-streptomycin at 37 °C in 5% CO_2 atmosphere.

2.6 *In-vitro* cytotoxicity assay

The cytotoxicity of AIE-CNPy-AD was investigated by Cell Counting Kit-8 (CCK-8) assay (Dojindo, Japan) according to the instruction manual. Briefly, human neuroblastoma cells (SH-SY5Y cells) were seeded into a 96-well plate at a density of 5000 cells/well for 24 h. Serial concentrations of AIE-CNPy-AD (0–32 μM, 200 μL/well) were added to treat cells. After being incubated for 24 h, culture medium with AIE-CNPy-AD was withdrawn, and then a fresh medium containing 10 μL of CCK-8 reagent was added to each well. Cells were incubated for another 3 h at 37 °C in 5% CO_2 atmosphere. The absorbance at 450 nm was measured by a micro-plate reader (SpectraMAX 190, Molecular Devices). The cell viability was calculated using GraphPad Prism 7.0 software. The cytotoxicity assay procedures of mouse brain neuroblastoma cells (Neuro-2a), mouse breast cancer cells (4T1), and human breast cancer cells (MCF-7) are the same as that of SH-SY5Y, except that the number of the other three cells inoculated in 96-well plates was 10,000 cells/well.

2.7 Animals

5*FAD transgenic mice (C57BL/6J, 2, 2.5-month-old), APP/PS1 transgenic mice (C57BL/6J, 2, 3, 4, and 6-month-old) and age-matched wild-type mice (C57BL/6J, 2, 2.5, 3, 4, and 6-month-old) were purchased from Zhishan (Beijing) Institute of Health Medicine Co., Ltd. (Beijing, China). Care and handlings of all mice adhered to the approval of Institutional Animal Care and Use Committee of East China University of Science & Technology (Assigned approval no: ECUST-2020-04014).

2.8 *In-vitro* fluorescence staining of mice brain slices using AIE-CNPy-AD

In-vitro fluorescence staining of mice brain slices was performed to verify the binding ability of AIE-CNPy-AD to Aβ_{1-42} aggregates. 5*FAD transgenic mice, APP/PS1 transgenic mice and age-matched wild-type mice were sacrificed with cold saline perfusion for 15 min without administration of AIE-CNPy-AD. Brain tissues were dissected, fixed in 4% paraformaldehyde overnight, and dehydrated in 30% sucrose. Then the tissues were embedded with paraffin cut into 8 μm serial sections, and stored at –80 °C before use. Pre-prepared paraffin-embedded 4 μm brain tissue sections from 5*FAD transgenic mice (C57BL/6J, 2.5-month-old), APP/PS1 transgenic mice (C57BL/6J, 2, 3, 4, and 6-month-old) and age-matched wild-type mice (C57BL/6J, 2, 2.5, 3, 4, and 6-month-old) were used for *in-vitro* fluorescence staining. The tissue slices were baked in an incubator at 60 °C for 60 min to prevent stripping. After being cooled to room temperature, the slices were deparaffinized *via* immersion in xylene, followed by washing with different gradients of ethanol and water. Then the sections were heated to 95 °C in ethylene diamine tetraacetic acid (EDTA) antigen retrieval buffer for 20 min. After cooling, the sections were incubated in the aqueous solution of AIE-CNPy-AD (100 μM) at 37 °C for 20 min, and then washed with PBS buffer. The sections were blocked with 3% bovine serum albumin (BSA) solution at 37 °C for 60 min, permeabilized with 0.1% (*v*/*v*) Triton X-100 for 3 min at room temperature, and then incubated with anti-beta amyloid 1-42 antibody [mOC64] (ab201060, diluted by 1:200 with PBS buffer) at 4 °C overnight. Sections that were incubated only with 3% BSA served as controls. After being washed 3 times with PBS buffer, all sections were stained with Alexa Fluor® 488-labeled goat anti-rabbit secondary antibody (ab150077, 1:1000) at 37 °C for 60 min. After being washed 3 times with PBS buffer, anti-fluorescence quenching mounting solution containing Hoechst 33342 was added. Finally, samples were observed under a confocal laser scanning microscope (CLSM, Heidelberg, Germany), using the following conditions: Hoechst 33342: λ_{ex} = 405 nm, λ_{em} = 461 nm; Alexa Fluor® 488: λ_{ex} = 488 nm, λ_{em} = 519 nm; AIE-CNPy-AD: λ_{ex} = 488 nm, λ_{em} = 620 nm.

2.9 Real-time *in-vivo* imaging in transgenic mice

The live imaging experiments were conducted to observe the distribution of AIE-CNPy-AD in brains. Before *in-vivo* imaging, the heads of transgenic mice of different ages and age-matched wild-type mice were shaved and cleaned. The background fluorescence was captured by LivingImage system before the administration of AIE-CNPy-AD. Then AIE-CNPy-AD was injected to transgenic mice and age-matched wild-type mice (*n*=3 for APP/PS1 transgenic mice, *n*=2 for 5*FAD transgenic mice) *via* tail vein (2.0 mg/kg, 5.5% dimethyl sulfoxide (DMSO), 94.5% PBS buffer, 400 μL). Then mice were anaesthetized by isoflurane and photographed by LivingImage system at pre-set time points (λ_{ex} = 500 nm, λ_{em} = 620 nm). The relative fluorescence intensity was analyzed by LivingImage 4.3.1 software (Caliper).

2.10 Evaluation of the *in-vivo* biocompatibility of AIE-CNPy-AD

5*FAD (2-month-old), APP/PS1 (6-month-old) transgenic mice, and wild-type mice (6-month-old) were chosen as

models and were injected with AIE-CNPy-AD or PBS buffer *via* tail vein injection, then sacrificed with cold saline perfusion at 24 h after administration. Heart, liver, spleen, lung, kidney, and brain tissues were dissected from the above mice, fixed in 4% paraformaldehyde overnight, and dehydrated in 30% sucrose. Then the tissues were embedded with paraffin cut into 8 μm serial sections, and stored at –80 °C before use. All the tissue slices were observed using hematoxylin-eosin staining. The brain slices were also observed utilizing TdT-mediated DUTP Nick-End Labeling (Tunel) technique to detect the apoptosis.

2.11 *Ex-vivo* observation for fluorescence signals of the brain slices of mice intravenously injected with AIE-CNPy-AD

APP/PS1 transgenic mice of different ages and age-matched wild-type mice were injected with AIE-CNPy-AD, then sacrificed with cold saline perfusion at 15 min after administration. Brain tissues were dissected, fixed in 4% paraformaldehyde overnight, and dehydrated in 30% sucrose. Then the tissues were embedded with optimum cutting temperature embedding medium (OCT), cut into 8 μm serial sections, and stored at –80 °C before use. The sections were blocked with 3% BSA solution at 37 °C for 60 min, permeabilized with 0.1% (*v*/*v*) Triton X-100 for 3 min at room temperature, then incubated with anti-beta amyloid 1-42 antibody [mOC64] (ab201060) overnight at 4 °C. After being washed for 3 times with PBS buffer, all sections were stained with Alexa Fluor® 488-labeled goat anti-rabbit secondary antibody at 37 °C for 60 min, followed by the addition of anti-fluorescence quenching mounting solution containing Hoechst 33342. Finally, samples were observed with a confocal laser scanning microscope (CLSM, Heidelberg, Germany). (Hoechst 33342: λ_{ex} = 405 nm, λ_{em} = 461 nm; Alexa Fluor® 488: λ_{ex} = 488 nm, λ_{em} = 519 nm; AIE-CNPy-AD: λ_{ex} = 488 nm, λ_{em} = 620 nm).

2.12 Docking simulations and analysis

The structure of AIE-CNPy-AD was optimized with a B3LYP/6-31+G* basis set using the Gaussian 09 package [42]. The structures of the Aβ_{1-42} fibrils (PDB ID: 2BEG [43]) and the Aβ_{1-42} monomer (PDB ID: 1Z0Q [44]) were obtained from the Protein Data Bank [45]. AutoDockTools 1.5.7 [46] was employed to molecular docking simulation and the dimensions of the grids were 126 Å × 68 Å × 74 Å for Aβ fibrils (spacing: 0.375 Angstrom) and 126 Å × 64 Å × 60 Å for Aβ monomers (spacing: 0.464 Angstrom). We used the Lamarckian genetic algorithm and a standard protocol to conduct calculations on the binding energies and modes of AIE-CNPy-AD to Aβ fibrils or Aβ monomer. The calculation results were analyzed by PyMOL (version 2.3.1) [47].

3 Results and discussion

3.1 Rational design and facile synthesis of AIE-CNPy-AD

We made full use of the "multi-pronged" strategy to pursue high-performance probes for early *in-situ* tracing of Aβ deposits *in vivo*. As introduced above, extended D-π-A electronic architecture is built by utilizing the dimethylamino as electron-donor, the acetonitrile and pyridyl group as electron-acceptor, single bonds as linkers, and benzyl groups and C=C double bond as π-bridges, respectively. Red or even NIR emission and relatively long-wavelength excitation is supposed to result from this D-π-A structured backbone. Such a rod-like geometric configuration is envisioned to bestow the probe with strong binding affinity to Aβ deposits. Moreover, according to the principle of restriction of intramolecular motions (RIM), the multiple rotors in the skeleton would efficiently consume the excited-state energy and lead to weak or even no emission in the unconstrained state, while the distorted 3D conformation would prevent π-π stacking and self-quenching in the constrained state. It means such an AIE-active probe would give light-up response to the target species with satisfactory SNR under suitable conditions. To further reinforce the SNR, hydrophilic propanesulfonate group is incorporated to the hydrophobic skeleton to for one thing enhance the solubility of the probe in aqueous media and thus reduce the background/noise signal, and for another to strengthen the binding between the probe and Aβ deposits *via* multiple non-covalent interactions. Moreover, the considerable lipophilicity of the AIE-CNPy-AD is anticipated to be sufficient to ensure desirable BBB penetrability. The elaborately designed rod-like amphiphilic red/NIR-emissive zwitterionic AIE probe AIE-CNPy-AD was conveniently synthesized according to the synthetic route shown in Figure S1 with commercially available cheap raw materials. AIE-CNPy-AD was fully characterized with the help of ^{1}H NMR (Figure S2), ^{13}C NMR (Figure S3) and high-resolution mass spectrometry (HRMS, Figure S4).

3.2 Outstanding photophysical properties facilitating the detection of Aβ deposits

AIE-CNPy-AD showed an absorption maximum at 455 nm and an emission maximum at 720 nm (10^{-4} M) in DMSO solution (Figure 2a), with the Stokes shift of as large as 265 nm. As AIE-CNPy-AD is soluble in highly polar solvents but aggregates in less polar solvents, DMSO was chosen as a good solvent, and THF was selected as a poor solvent to evaluate the AIE behaviors of AIE-CNPy-AD (Figure 2 and Figure S5). As anticipated, with the addition of THF, fluorescence enhancement was clearly observed, with the emission peak blue-shifted from 720 nm (DMSO solution) to 675 nm (DMSO/THF = 1/99, *v*/*v*), manifesting the

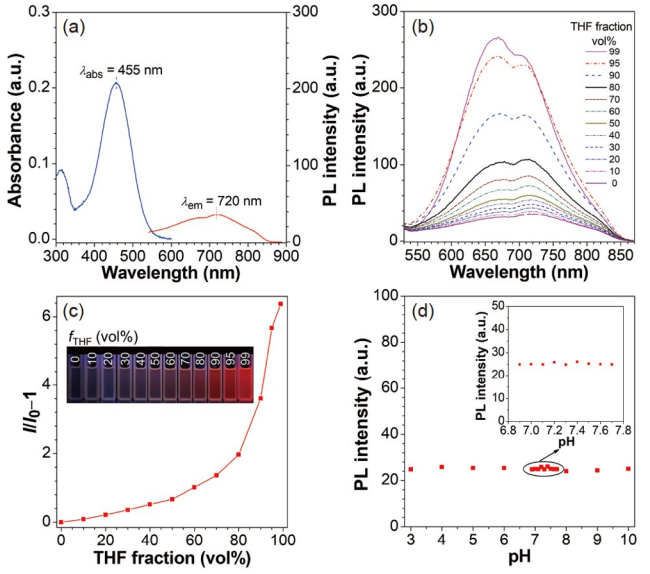

Figure 2 The photophysical properties of AIE-CNPy-AD. (a) Absorption ($c = 10^{-5}$ M) and emission spectra (λ_{ex} = 455 nm, $c = 10^{-4}$ M) of AIE-CNPy-AD in the DMSO solution at room temperature. (b) Emission spectra of AIE-CNPy-AD in the DMSO/THF mixtures with different THF fractions at room temperature (λ_{ex} = 455 nm, $c = 10^{-5}$ M). (c) The plot of the emission enhancement (I/I_0–1) *versus* the THF fractions. The inset: corresponding fluorescent photographs of AIE-CNPy-AD in the DMSO/THF mixtures with different THF fractions taken under the irradiation at 365 nm with a handheld UV lamp. (d) Maximum fluorescence intensity of AIE-CNPy-AD keeping unchanged under different pH values (color online).

synergistic effect of AIE and intramolecular charge transfer (ICT) (Figure 2b). The emission intensity continuously increased slowly when the THF fraction (f_{THF}) was no more than 60 vol%, while boosted sharply once f_{THF} reached 70 vol% (Figure 2c). Remarkably, AIE-CNPy-AD was hardly affected by the pH value varying from 3 to 10 covering the normal pH range of human body (Figure S6 and Figure 2d), suggesting the good pH stability of the fluorescence emission properties of our probe. Taken together, all these results undoubtedly demonstrated the remarkable AIE feature, strong ICT effect, and the stable red/NIR fluorescence in the aggregated state of AIE-CNPy-AD, which are conducive to the imaging of Aβ deposits.

3.3 High specificity and affinity of AIE-CNPy-AD to Aβ fibrils

The binding affinity of AIE-CNPy-AD to hen egg white lysozyme (HEWL), a common model protein for amyloid studies, was evaluated first. As shown in Figure 3a, dramatic fluorescence enhancement at 620 nm was clearly observed with the increasing concentration of fibrillar HEWL in the PBS solution. In sharp contrast, AIE-CNPy-AD displayed much less marked fluorescence response to native HEWL at the same concentration level (Figure S7A). As compared with the emission in DMSO solution, the probe bound to HEWL showed an emission peak blue-shifted from 720 to 620 nm, which might be attributed to the ICT effect and less polar microenvironment of the protein pockets. To our satisfaction, AIE-CNPy-AD has much higher ability to distinguish fibrillar HEWL from native ones, as ThT had the same response to both fibrillar and native HEWL (Figure 3b, c, and Figure S7B). Moreover, due to the strong ACQ effect of indocyanine green (ICG), even a small amount of fibrillar HEWL would prompt the quenching of fluorescence (Figure S7C and Figure 3c), making it unworkable in the detection of fibrillar HEWL. These results suggest that AIE-CNPy-AD possesses higher possibility to function as a highly specific probe to Aβ fibrils in comparison to widely used gold standard fluorescent probes such as ThT.

We then studied whether this AIE-active NIR probe could have a specific fluorescence response to Aβ fibrils. Aβ_{1-42} peptide was fully incubated to afford Aβ_{1-42} fibrils with expected fibrous or filamentous structure (Figure 3d). When the Aβ_{1-42} fibrils were added, emission intensity of AIE-CNPy-AD increased consistently with the emission peak blue-shifted to 620 nm like the situation of binding to HEWL (Figure 3e). Obviously, the background from AIE-CNPy-AD is far lower than that of ThT, which is merely 1/35 times that of ThT. Whereas, the signal of AIE-CNPy-AD upon interaction with Aβ_{1-42} fibrils is much higher than that of ThT under parallel conditions, which is about 1.4 times that of ThT (Figure S8). In consequence, the SNR of AIE-CNPy-AD reached 60, which is 10 times to that of ThT (SNR_{ThT} = 6; Figure 3f). The significantly enhanced SNR of AIE-CNPy-AD achieved by the minimization of background and amplification of signal could be interpreted as follows: (i) on one hand, the right hydrophilicity makes the AIE-CNPy-AD well dispersed in aqueous solution and the vigorous intramolecular motions efficiently exhaust the excited state, resulting in minimal emission; (ii) on the other hand, the strong binding of AIE-CNPy-AD to Aβ_{1-42} fibrils greatly hampered the intramolecular motions and activated the radiative decay channels, maximizing the fluorescence signal as a consequence of AIE effect. Highly sensitive detection of Aβ_{1-42} fibrils could thus be expected.

In addition to the considerably high SNR, AIE-CNPy-AD also has high specificity to Aβ_{1-42} fibrils. A large variety of biological species including carbohydrates, amino acids, peptides, and other proteins were employed to assess specificity of AIE-CNPy-AD to Aβ_{1-42} fibrils (Figure 3g, Figure S9). It is evident that AIE-CNPy-AD not only hardly has response to interfering small molecular species, but also has low response to potentially competitive peptides and enzymes with large molecular weight, especially Aβ_{1-42} monomer (Figure 3g and Figure S9).

Apart from specificity, binding affinity of the probe to analyte is also a vital parameter that ensures accurate tracing of the Aβ_{1-42} fibrils. Displacement assay of AIE-CNPy-AD against ThT-bound Aβ_{1-42} fibrils (Figure S10 and Figure 3h)

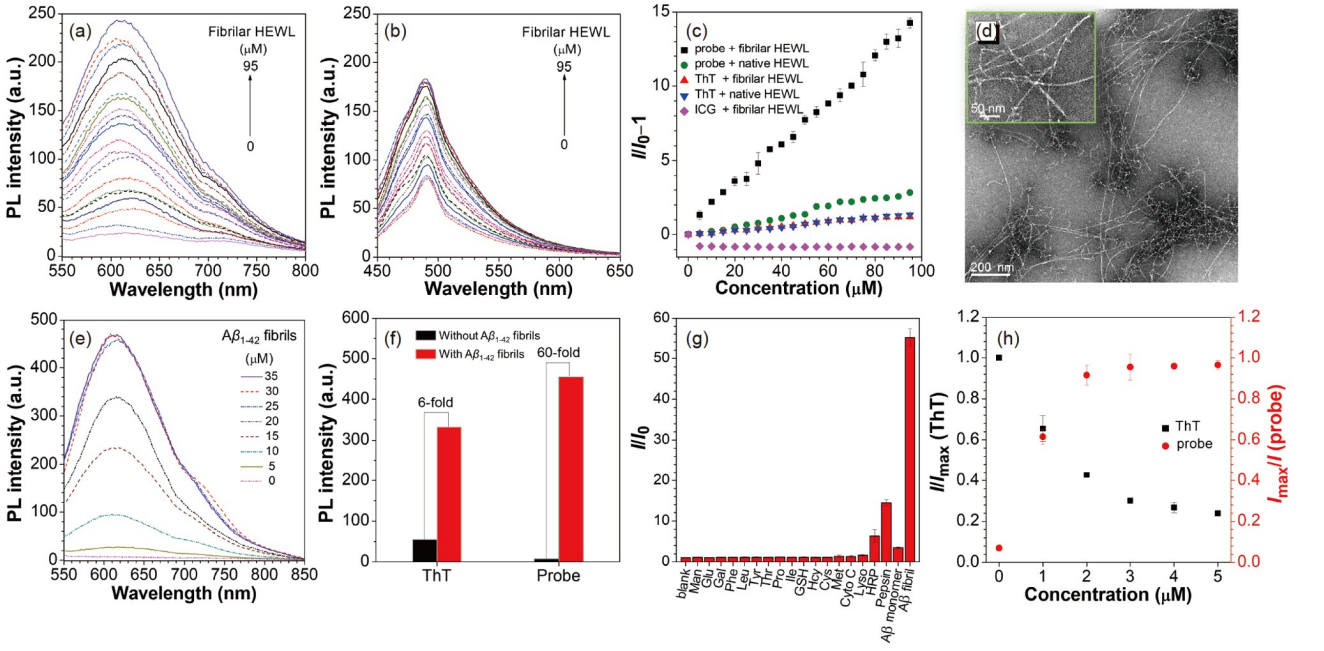

Figure 3 Evaluation on the specificity and affinity of AIE-CNPy-AD to Aβ fibrils. Emission spectra of (a) AIE-CNPy-AD (λ_{ex} = 455 nm, c = 5 μM) and (b) ThT (λ_{ex} = 420 nm, c = 5 μM) in PBS solution (pH = 7.4, containing 0.5% DMSO) with stepwise addition of fibrillar HEWL (0–95 μM). (c) The plots of I/I_0-1 of probe AIE-CNPy-AD, ThT and ICG *versus* different concentrations of fibrillar HEWL and native HEWL, c = 5 μM. (d) TEM images of pre-formed Aβ_{1-42} fibrils. Inset: the enlarged TEM image of the Aβ_{1-42} fibrils. (e) Emission spectra of AIE-CNPy-AD in PBS solution (pH = 7.4) with stepwise addition of Aβ_{1-42} fibrils, λ_{ex} = 455 nm, c = 5 μM. (f) Fluorescence intensity of ThT and AIE-CNPy-AD bound with or without Aβ_{1-42} fibrils, respectively. (g) I/I_0 response assay *versus* various analytes. (h) The plot of I_{max}/I of AIE-CNPy-AD and I/I_{max} of ThT *versus* different concentrations of AIE-CNPy-AD (color online).

was then carried out to investigate the binding affinity. Fluorescence intensity of the pre-prepared ThT/Aβ_{1-42} fibrils complex was firstly recorded with excitation at 420 nm. AIE-CNPy-AD solution was subsequently added stepwise into the ThT/Aβ_{1-42} complex, and the emission intensities of these two probes were measured under excitation at their corresponding maximum absorption wavelengths. It is observed that the emission intensity of ThT at 482 nm decreased continuously with increasing concentration of AIE-CNPy-AD; and in the meantime, fluorescence of AIE-CNPy-AD peaked at 620 nm emerged and was enhanced accordingly. Remarkably, it is indicated that AIE-CNPy-AD displaced ThT from ThT/Aβ fibrils complex to generate the more strongly bound AIE-CNPy-AD/Aβ fibrils complex in the solution. Besides, dissociation constant (K_d) [23] of AIE-CNPy-AD was calculated to be 185 nM (Figure S11), considerably smaller than that of ThT (890 nM) [24]. Sufficient evidences proved that AIE-CNPy-AD has much higher binding affinity to Aβ_{1-42} fibrils than ThT.

3.4 High-contrast and high-resolution *in-vitro* fluorescent staining of paraffin slices of mouse brains

It is confirmed that AIE-CNPy-AD, with high specificity, binding affinity and SNR, exhibits high performance on precise detection of Aβ_{1-42} fibrils in solution. To explore the ability of AIE-CNPy-AD labelling Aβ deposits in brain tissues, *in-vitro* fluorescent staining of paraffin mice brain slices resected from 5*FAD transgenic mice, APP/PS1 transgenic mice and age-matched wild-type mice was conducted with AIE-CNPy-AD. False signals originating from the binding of AIE-CNPy-AD or antibody with proteins or interfering species in brain cells could be identified through the localization of nuclei with Hoechst 33342. Notably, as displayed in Figure 4 and Figure S12, either in 2.5-month-old 5*FAD transgenic mice or in 6-month-old APP/PS1 transgenic mice, Aβ deposits were unambiguously visualized with bright red fluorescence. Specific labelling of Aβ deposits with high contrast and high resolution in these mice indicates that AIE-CNPy-AD is universal to label Aβ deposits in different strains of mice. Moreover, it can be easily seen from the CLSM images, the Aβ deposits in 2.5-month-old 5*FAD transgenic mice (Figure 4a and Figure S12A–C) are larger and more densely distributed than that in 6-month-old APP/PS1 transgenic mice (Figure 4f and Figure S12D–F). The experimental results agreed well with situation of early deposit formation at the time point in these two strains of mice [2,48], implying the reliability of AIE-CNPy-AD in fluorescent staining of Aβ deposits in slices of mice brain. To our delight, there was no observable intracell fluorescence signal, which implied that our probe is preferentially bound to the Aβ deposits generally forming extracellularly, eliminat-

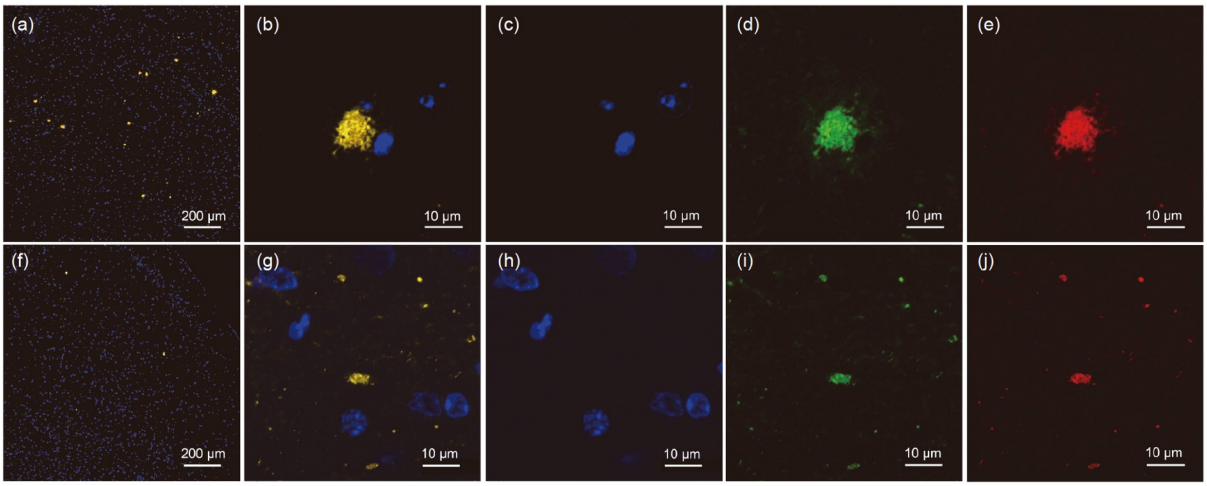

Figure 4 *In-vitro* fluorescent staining of paraffin slices of mice brains. Fluorescent staining of the brain slices of 2.5-month-old 5*FAD transgenic mice (a–e) and 6-month-old APP/PS1 transgenic mice (f–j). The slices were co-stained with AIE-CNPy-AD, anti-beta amyloid 1-42 [mOC64] (ab201060), Alexa Fluor® 488-labeled goat anti-rabbit secondary antibody (ab150077), and Hoechst 33342 in sequence. (a, b, f, g) Merged images of three channels; (c, h) blue channel: Hoechst 33342, λ_{ex} = 405 nm, λ_{em} = 461 nm; (d, i) green channel: Alexa Fluor® 488, λ_{ex} = 488 nm, λ_{em} = 519 nm; (e, j) red channel: AIE-CNPy-AD, λ_{ex} = 488 nm, λ_{em} = 620 nm. (a, f) 100× magnification, (b–e, g–j) 2000× magnification (color online).

ing the false signal from intracellular species. Simultaneously, the signals in the red channel in agreement with those in the green channel manifested that AIE-CNPy-AD has quite high specificity comparable to that of antibody to Aβ deposits (Figure 4b–e, g–j). In contrast to transgenic mice, no deposits were found in the age-matched wild-type mice observing from either red or green channel (Figure S13), which not only verified the high specificity of AIE-CNPy-AD to Aβ deposits for a second time, but also suggested the fairly high fidelity of the designed probe in real brain tissues.

3.5 *In-vivo* imaging of Aβ deposits in live mice with high signal-to-noise ratio

Inspired by the very good red fluorescence light-up Aβ deposit-specific response in the brain slices of mice, we further evaluated the biocompatibility and BBB penetrability of AIE-CNPy-AD, which is indispensable before *in-vivo* imaging. Cell viability experiments were first carried out to ascertain the biocompatibility of AIE-CNPy-AD by CCK-8 assays. Human neuroblastoma cells (SH-SY5Y), mouse brain neuroblastoma cells (Neuro-2a), mouse breast cancer cells (4T1) and human breast cancer cells (MCF-7) were incubated with different concentrations of AIE-CNPy-AD for 24 h, respectively. The cell viabilities of all these four cell lines both kept at a level close to 100% even at a probe concentration of 32 μM (Figure S14A–D). The results provided strong evidence to the fact that AIE-CNPy-AD has low cytotoxicity and favourable biocompatibility to various cells, demonstrating its high applicability to live animals. The oil-water partition coefficient (log*P*) is often used as an index indicating the possible ability of penetrating BBB [16]. The log*P* of AIE-CNPy-AD was determined to be 1.24 by shaking-flask method, which is far larger than that of ThT (0.16) [16], suggestive of the higher lipophilicity and BBB penetrating potential of AIE-CNPy-AD as compared with ThT.

The feasibility of AIE-CNPy-AD tracking Aβ deposits *in vivo* was confirmed using 2.5-month-old 5*FAD mice, 6-month-old APP/PS1 mice and age-matched wild-type mice as model mice. Live imaging of these mice was performed after the tail vein injection of AIE-CNPy-AD (Figure 5). Almost all the fluorescence signals were clearly witnessed in the center of brain compartments and able to be efficiently captured. Apparently, the fluorescence signals in the brain regions of 2.5-month-old 5*FAD mice (Figure 5a) were already much stronger than those in the wild-type mice at 5 min post injection (Figure 5b). Particularly, with the decay of signal, difference in signal intensity recorded from 5*FAD and wild-type mice was enlarged as indicated by the semi-quantitative analysis of the images (Figure 5c). Similarly, intense fluorescence signal is readily visible from the brain area of 6-month-old APP/PS1 mice after the injection of AIE-CNPy-AD. Moreover, the contrast between the fluorescence signals from APP/PS1 and 6-month-old wild-type mice is quite dramatic (Figure 5d, e). Compared with 5*FAD mice, difference in the signal intensity between APP/PS1 mice and age-matched wild-type mice was 4.7 times larger than that between 5*FAD mice and the corresponding wild-type mice at 5 min after being injected with AIE-CNPy-AD (Figure 5c, f). It might be because the formation of Aβ deposits in APP/PS1 mice is slower than that in 5*FAD mice. In addition, fluorescence signal intensity of APP/PS1 mice declined faster than that of 5*FAD mice after being injected with AIE-CNPy-AD for 30 min. It is possibly because there

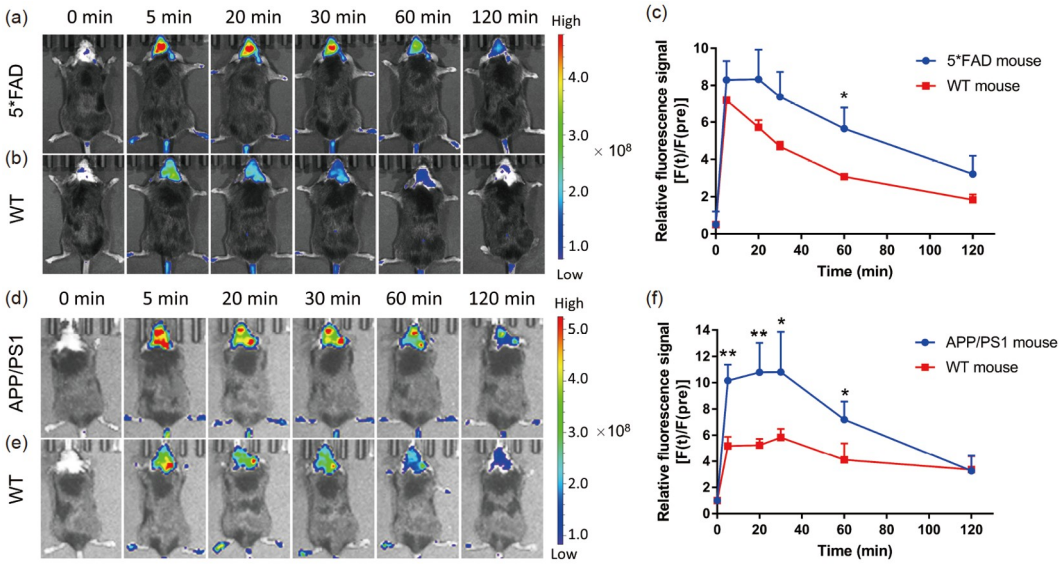

Figure 5 *In-vivo* imaging of Aβ plaques in live mice. Fluorescence images of (a) 5*FAD mice (2.5-month-old) and (b) wild-type mice (2.5-month-old) at different time points before and after *via* tail vein injection of AIE-CNPy-AD (2.0 mg/kg). (c) The relative fluorescence signal [F(t)/F(pre)] in the brain regions of 5*FAD mice and wild-type mice after *via* tail vein injection of AIE-CNPy-AD (2.0 mg/kg). Fluorescence images of (d) APP/PS1 mice (6-month-old) and (e) wild-type mice (6-month-old) at different time points before and after *via* tail vein injection of AIE-CNPy-AD (2.0 mg/kg). (f) The relative fluorescence signal [F(t)/F(pre)] in the brain regions of APP/PS1 mice and wild-type mice after *via* tail vein injection of AIE-CNPy-AD (2.0 mg/kg). λ_{ex} = 500 nm, λ_{em} = 620 nm. All data in (c) and (f) were displayed as mean ± s.d. Student's t test was used for comparison between two groups. *P < 0.05 was considered significant; **P < 0.01 was considered highly significant (color online).

are larger and more Aβ deposits in 2.5-month-old 5*FAD mice than in 6-month-old APP/PS1 mice, which slows down the clearance of AIE-CNPy-AD from the brain. Notably, either in 5*FAD mice or APP/PS1 mice at 1 h post probe injection, F(t)/F(Pre) value of transgenic mice was at least 1.75 times that of wild-type mice, indicative of the potential of AIE-CNPy-AD to realize long-term tracking of Aβ deposits *in vivo*. Undoubtedly, these visualization results directly validated that AIE-CNPy-AD is capable of penetrating the BBB and imaging Aβ deposits *in vivo* with high contrast and fidelity.

3.6 *In-vivo* tracking of Aβ deposits in APP/PS1 mice at an early stage

It has confirmed that AIE-CNPy-AD exhibits significant signal difference between transgenic mice and wild-type mice in a relatively long time-period post probe administration. It can be envisaged that AIE-CNPy-AD might be promising for early diagnosis of AD in transgenic mice by virtue of the Aβ deposits-specific *in-vivo* imaging ability of AIE-CNPy-AD. Young APP/PS1 transgenic mice of 2-month-, 3-month-, 4-month-, and 6-month-old and age-matched wild-type (WT) mice were thus employed to systematically assess the performance of AIE-CNPy-AD in early diagnosis of AD (Figure 6 and Figure S15). It was observed that the difference in the fluorescence signal intensity of APP/PS1 transgenic mice and wild-type mice already became very evident at the age of 4 month. In the meantime, the fluorescence signal intensity is positively correlated with the age of transgenic AD mice (Figure 6a). More specifically, at 20 min post injection, the F(t)/F(Pre) value of the 4-month-old APP/PS1 transgenic mice was 1.86 times that of the age-matched WT mice, and the F(t)/F(Pre) value of 6-month-old APP/PS1 transgenic mice was 2.06 times that of the age-matched WT mice (Figure 6b). Meanwhile, there was no apparent signal difference in WT mice of different months (Figure 6c), and the F(t)/F(Pre) values of 2-month-old and 3-month-old APP/PS1 transgenic mice were almost the same as those of the age-matched WT mice (Figure 6d). These imaging results especially those acquired with APP/PS1 transgenic mice at an age of 4-month-old clearly showed that AIE-CNPy-AD is competent for the precise diagnosis of AD at an early stage. It has been speculated that the reason for the failure of early drug intervention on AD is probably that intervention in the phase is not early enough, which in turn is greatly related to the efficient capture of biological manifestations rather than clinical manifestations in the early diagnosis [3,25]. The experimental results obtained with AIE-CNPy-AD is of great significance because APP/PS1 transgenic mice are found to exhibit memory deficits from 5 months old on, which is early clinical presentations, confirming that AIE-CNPy-AD can diagnose AD of APP/PS1 transgenic mice during the period of early biological manifestations, prior to the appearance of clinical presentations [2,3,26].

It is worth mentioning that AIE-CNPy-AD does not only hold satisfactory cytocompatibility with negligible toxicity

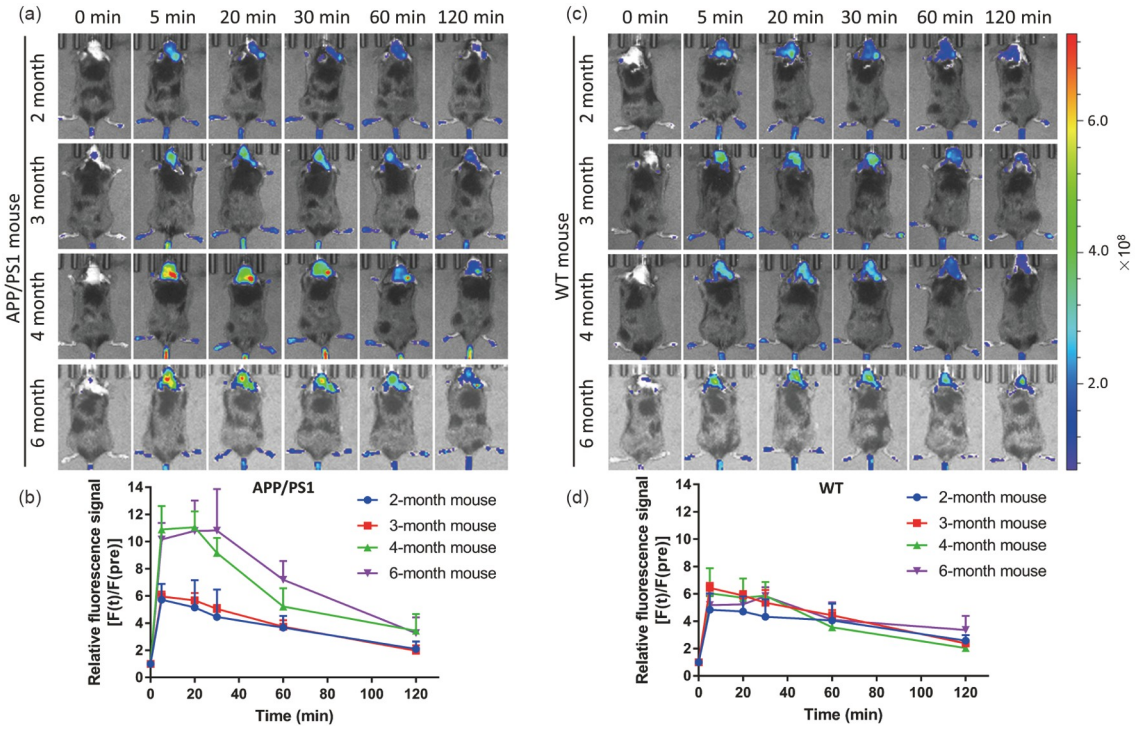

Figure 6 *In-vivo* tracking of A*β* plaques in APP/PS1 mice at different ages. Fluorescence images of APP/PS1 mice (a) or wild-type mice (c) of different ages (2-month-old, 3-month-old, 4-month-old, 6-month-old) at different time points taken before or at different time points after tail vein injection of AIE-CNPy-AD (2.0 mg/kg). The relative fluorescence signal [*F*(t)/*F*(pre)] in the brain regions of APP/PS1 mice (b) or wild-type mice (d) of different ages after *via* tail vein injection of AIE-CNPy-AD (2.0 mg/kg). AIE-CNPy-AD: λ_{ex} = 500 nm, λ_{em} = 620 nm (color online).

to diverse cells including neuronal cell lines but also has good *in-vivo* biocompatibility as suggested by Figure S16. The Haematoxylin and eosin (H&E) staining results of the heart, liver, spleen, lung, kidney, and brain slices resected from 5*FAD (2-month-old), APP/PS1 (6-month-old) transgenic mice, and wild-type mice (6-month-old) at 24 h post the administration with AIE-CNPy-AD *via* tail vein injection are almost identical to those injected with PBS buffer under parallel conditions. It manifests that AIE-CNPy-AD does not cause obvious necrosis to tissues, suggesting the good *in-vivo* biocompatibility of the present probe. The Tunel results of the brain slices further verifies this as there is no evident apoptosis being observed in all the samples. Therefore, in view of the very low toxicity to cells and tissues, the AIE-CNPy-AD is proven to be highly suitable for *in-vivo* detection and has great potential in clinical use.

3.7 *Ex-vivo* observation of frozen brain slices of mice pre-administrated with AIE-CNPy-AD further validates its high fidelity in A*β* deposits-specific imaging

To further examine whether the AIE-CNPy-AD binds exclusively to A*β* deposits in the brain of live mice, the APP/PS1 transgenic mice of different ages and age-matched wild-type mice were injected with AIE-CNPy-AD and sacrificed at 15 min post-administration. The frozen slices of these mouse brains were then stained with anti-beta amyloid 1-42 [mOC64] (ab201060), Alexa Fluor® 488-labeled goat anti-rabbit secondary antibody (ab150077), and Hoechst 33342 in sequence. As shown in Figure 7a, f, and Figure S16, the A*β* deposits were imaged with high resolution and high contrast. Moreover, it can be clearly observed that the A*β* deposits in brain slices of 6-month-old APP/PS1 transgenic mice were larger and richer in number than those of 4-month-old APP/PS1 transgenic mice, while no significant A*β* deposits were found in the brain slices of 2-month-old, 3-month-old APP/PS1 transgenic mice (Figure S17), and all the age-matched WT mice (Figure S18). Manifestly, AIE-CNPy-AD indeed labelled A*β* deposits *in vivo* with quite high fidelity and specificity, as suggested by the fairly good overlap between the green (antibody) and red channels (AIE-CNPy-AD; Figure 7b–e, g–j).

3.8 Elucidation of the working mechanism with molecular docking simulations

We believe that the rod-like architecture, extended D-π-A electronic structure, flexible 3D conformation, the amphiphilic and zwitterionic molecular structure collectively contribute to the high performance of AIE-CNPy-AD in A*β* deposits-specific detection and imaging. As above mentioned, the rod-like structure is supposed to favours the re-

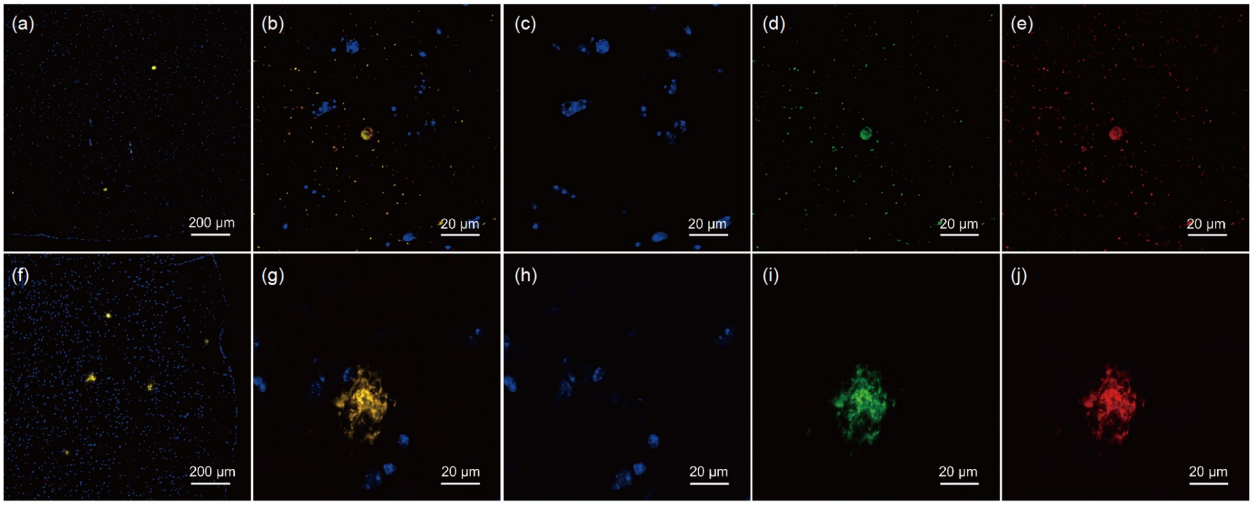

Figure 7 *Ex-vivo* observation of frozen brain slices of mice pre-administrated with AIE-CNPy-AD. Fluorescent staining of the brain slices of 4-month-old APP/PS1 transgenic AD mice (a–e) and 6-month-old APP/PS1 transgenic AD mice (f–j). The slices of mice were pre-injected with AIE-CNPy-AD *via* tail vein injection, and then sequentially stained with anti-beta amyloid 1-42 [mOC64] (ab201060) and Alexa Fluor® 488-labeled goat anti-rabbit secondary antibody (ab150077) after sacrificing. (a, b, f, g) Merged image of three channels; (c, h) blue channel: Hoechst 33342, λ_{ex} = 405 nm, λ_{em} = 461 nm; (d, i) green channel: Alexa Fluor® 488-labeled antibody, λ_{ex} = 488 nm, λ_{em} = 519 nm; (e, j) red channel: AIE-CNPy-AD, λ_{ex} = 488 nm, λ_{em} = 620 nm. (a, f) 100× magnification; (b–e, g–j) 1000× magnification (color online).

cognition of β sheets. Moreover, the hydrophobic π-conjugated backbone and the pyridyl and sulfonate groups are envisaged to benefit the binding of AIE-CNPy-AD to Aβ species possibly *via* hydrophobic interaction, π-π interaction, and electrostatic interaction. When in solution or molecularly dispersed, the AIE-CNPy-AD molecules undergo active intramolecular motions, leading to an OFF state and a low background. When coexists with Aβ monomer, intramolecular motions of AIE-CNPy-AD are merely weakly restricted, rendering weak red emission released (near-OFF state), due to the weak binding affinity of AIE-CNPy-AD and Aβ monomer. On the contrary, strong interactions between AIE-CNPy-AD and deposits impose severe restriction on the intramolecular motions, which activates the AIE process [27,28,30,32,33], and switches AIE-CNPy-AD from OFF to ON state to emit strong red/NIR fluorescence. Thus, AIE-CNPy-AD can distinguish Aβ deposits from Aβ monomers precisely (Figure 8a).

Molecular docking simulations were carried out to unveil the interactions between AIE-CNPy-AD and Aβ fibrils or monomer and to elucidate the working mechanism of specific detection of Aβ fibrils. As revealed by the three top docking conformations with the lowest binding free energies shown in Figure 8b, c and Figure S19, the most preferable binding direction of AIE-CNPy-AD to Aβ fibrils is consistent with the orientation of the β-sheets of Aβ fibrils, which proves that rod-shaped geometric structure of AIE-CNPy-AD is very helpful to the binding with Aβ fibrils. Simultaneously, the hydrophobic PHE-19 residue on the β-sheets of Aβ fibrils has strong C–H···π interaction (2.6 Å) with the phenyl ring of AIE-CNPy-AD, and the ALA-21 residue exhibits very strong interaction with the cyano group of AIE-CNPy-AD (2.2 Å). To our astonishment, the GLY-25 residue and two LYS-28 residues have strong hydrogen bonding interactions with the sulfonate group of AIE-CNPy-AD (1.7–2.1 Å). It is obvious that sulfonate not only improves water solubility of AIE-CNPy-AD, but also further enhances the binding ability of AIE-CNPy-AD to Aβ deposits *via* H-bonding and electrostatic interactions. Collectively, the strong intermolecular interactions between AIE-CNPy-AD and Aβ fibrils greatly hinder the intramolecular motions of AIE-CNPy-AD to give out the "lighted-up" fluorescent response.

In contrast, only the LYS-28 residue of Aβ monomer shows hydrogen bonding interaction with the sulfonate unit of AIE-CNPy-AD and no other interactions exist, which results in weaker restriction on the intramolecular motions and weak fluorescence (Figure 8d, e). The inhibition constant (K_i) [49] of AIE-CNPy-AD and Aβ fibrils (935 nM) is far smaller than that of AIE-CNPy-AD and Aβ monomer (45.0 μM). Simultaneously, the lowest docking energy of AIE-CNPy-AD and Aβ fibrils was calculated to be −8.23 kcal/mol, which is substantially lower than that of AIE-CNPy-AD and Aβ monomer (−5.93 kcal/mol). As exhibited in Table S1 (Supporting Information online), all the ten best binding poses with the lowest energies of AIE-CNPy-AD and Aβ fibrils consistently display lower docking energies than those of AIE-CNPy-AD and Aβ monomer. These data sufficiently suggested that binding affinity of AIE-CNPy-AD to Aβ fibrils is much stronger than that of AIE-CNPy-AD to Aβ monomer. Moreover, the binding energy of AIE-CNPy-AD and Aβ fibrils is lower than that of ThT and Aβ

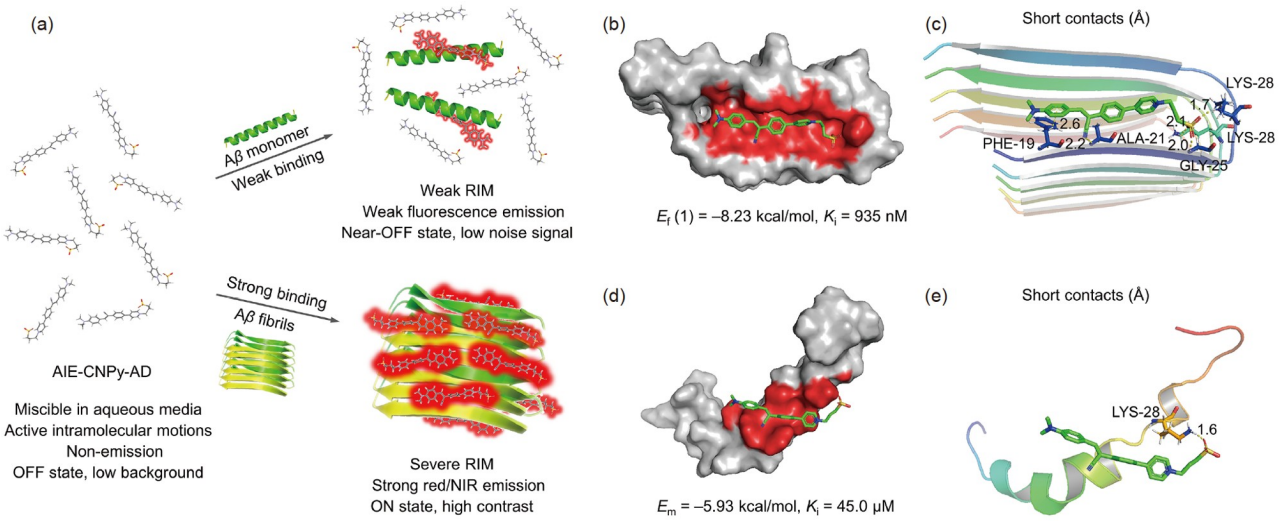

Figure 8 Working mechanism elucidated by molecular docking simulations. (a) Possible working mechanism of AIE-CNPy-AD in the specific detection of Aβ fibrils. The lowest energy binding mode of AIE-CNPy-AD with Aβ fibrils (PDB ID: 2BEG) in surface representation (b) [50] and cartoon representation (c). The lowest energy binding mode of AIE-CNPy-AD with Aβ monomer (PDB ID: 1Z0Q) in surface representation (d) and cartoon representation (e). E_f: binding energy of AIE-CNPy-AD with Aβ fibrils; E_m: binding energy of AIE-CNPy-AD with Aβ monomer. K_i is the inhibition constant (color online).

deposits (−7.18 kcal/mol) [11], indicating that the AIE-CNPy-AD possesses higher affinity to Aβ deposits as compared with ThT. The molecular docking simulation results are powerful proofs to our experiment results and further verify the rationality and feasibility of our design strategy.

4 Conclusions

Precise *in-vivo* tracking of Aβ deposits is of great significance to both fundamental research and technological development. In this work, we facilely developed a novel AIE-active red/NIR-emissive probe (AIE-CNPy-AD) for specifically discriminating and imaging Aβ deposits *in vivo* at an early stage. Rod-shaped amphipathic AIE-CNPy-AD possesses good BBB penetrability and high binding affinity to Aβ deposits. The extended D-π-A electronic structure with multiple rotors and flexible 3D conformations endues AIE-CNPy-AD with red/NIR emission, AIE feature, and resultant high *in-vivo* tracing capability of Aβ deposits with high deep-tissue penetrating ability, high signal-to-noise ratio, and high fidelity. More importantly, our probe also enjoys the following advantages (Table S2): (1) it is simple in structure, facile in preparation with cheap raw materials, and low in cost; (2) the *in-vivo* imaging capability is universal and not restricted by the strain of mouse; (3) the precise *in-vivo* tracking of Aβ deposits could be realized at a very early stage before the occurrence of clinical manifestations; (4) the probe maps the Aβ deposits at the earliest stage as compared with all the reported fluorescent probes; (5) the cyto-compatibility and *in-vivo* compatibility is satisfactory for *in-vivo* investigation and clinical application. Moreover, the rationality and feasibility were fully verified, and the working mechanism of AIE-CNPy-AD was elucidated by the molecular docking simulation results. The present work will not only shed light on the rational design of high-performance fluorescent probes for accurate imaging of Aβ deposits *in vivo*, but also provide a promising tool to diagnose AD at an early stage and find timing of early drug intervention.

Acknowledgements This work was supported by the National Natural Science Foundation of China (21788102, 21875064, 81903545, 21604023, 21790361), Shanghai Science and Technology Commission Basic Project-Shanghai Natural Science Foundation (21ZR1417600), Shanghai Municipal Science and Technology Major Project (2018SHZDZX03), Programme of Introducing Talents of Discipline to Universities (B16017), Shanghai Science and Technology Committee (17520750100), Beijing New-Star Plan of Science and Technology (Z201100006820009), Shanghai Sailing Program (16YF1402200), and the Fundamental Research Funds for the Central Universities.

Conflict of interest The authors declare no conflict of interest.

Supporting information The supporting information is available online at http://chem.scichina.com and http://link.springer.com/journal/11426. The supporting materials are published as submitted, without typesetting or editing. The responsibility for scientific accuracy and content remains entirely with the authors.

1 Panza F, Lozupone M, Logroscino G, Imbimbo BP. *Nat Rev Neurol*, 2019, 15: 73–88
2 Zhu S, Wang J, Zhang Y, He J, Kong J, Wang JF, Li XM. *CNS Neurosci Ther*, 2017, 23: 310–320
3 Fan DY, Wang YJ. *Neurosci Bull*, 2020, 36: 195–197
4 Jagust WJ, Landau SM. *Neurology*, 2021, 96: e1347–e1357
5 van Harten AC, Wiste HJ, Weigand SD, Mielke MM, Kremers WK, Eichenlaub U, Dyer RB, Algeciras-Schimnich A, Knopman DS, Jack CR, Petersen RC. *Alzheimers & Dement*, 2021, alz.12406

6 Ma X, Wang Y, Hua J, Xu C, Yang T, Yuan J, Chen G, Guo Z, Wang X. *Sci China Chem*, 2020, 63: 73–82
7 Aliyan A, Cook NP, Martí AA. *Chem Rev*, 2019, 119: 11819–11856
8 Jun YW, Cho SW, Jung J, Huh Y, Kim YS, Kim D, Ahn KH. *ACS Cent Sci*, 2019, 5: 209–217
9 Sabri O, Sabbagh MN, Seibyl J, Barthel H, Akatsu H, Ouchi Y, Senda K, Murayama S, Ishii K, Takao M, Beach TG, Rowe CC, Leverenz JB, Ghetti B, Ironside JW, Catafau AM, Stephens AW, Mueller A, Koglin N, Hoffmann A, Roth K, Reininger C, Schulz-Schaeffer WJ. *Alzheimers & Dement*, 2015, 11: 964–974
10 Cai J, Yi P, Miao Y, Liu J, Hu Y, Liu Q, Feng Y, Chen H, Li L. *ACS Appl Mater Interfaces*, 2020, 12: 26812–26821
11 Zhao DS, Chen YX, Liu Q, Zhao YF, Li YM. *Sci China Chem*, 2011, 55: 112–117
12 Hatai J, Motiei L, Margulies D. *J Am Chem Soc*, 2017, 139: 2136–2139
13 Staderini M, Martín MA, Bolognesi ML, Menéndez JC. *Chem Soc Rev*, 2015, 44: 1807–1819
14 Shin J, Verwilst P, Choi H, Kang S, Han J, Kim NH, Choi JG, Oh MS, Hwang JS, Kim D, Mook-Jung I, Kim JS. *Angew Chem Int Ed*, 2019, 58: 5648–5652
15 Law ASY, Lee LCC, Yeung MCL, Lo KKW, Yam VWW. *J Am Chem Soc*, 2019, 141: 18570–18577
16 Fu W, Yan C, Guo Z, Zhang J, Zhang H, Tian H, Zhu WH. *J Am Chem Soc*, 2019, 141: 3171–3177
17 Cui M, Ono M, Watanabe H, Kimura H, Liu B, Saji H. *J Am Chem Soc*, 2014, 136: 3388–3394
18 Zhou K, Bai H, Feng L, Dai J, Cui M. *Anal Chem*, 2017, 89: 9432–9437
19 Peng C, Wang X, Li Y, Li HW, Wong MS. *J Mater Chem B*, 2019, 7: 1986–1995
20 Yan JW, Zhu JY, Zhou KX, Wang JS, Tan HY, Xu ZY, Chen SB, Lu YT, Cui MC, Zhang L. *Chem Commun*, 2017, 53: 9910–9913
21 Fu H, Peng C, Liang Z, Dai J, Liu B, Cui M. *Chem Commun*, 2016, 52: 12745–12748
22 Cheng Y, Zhu B, Deng Y, Zhang Z. *Anal Chem*, 2015, 87: 4781–4787
23 Rajasekhar K, Narayanaswamy N, Murugan NA, Kuang G, Ågren H, Govindaraju T. *Sci Rep*, 2016, 6: 23668
24 Diner I, Dooyema J, Gearing M, Walker LC, Seyfried NT. *Bioconj Chem*, 2017, 28: 2627–2637
25 Liu B, Shen H, Hao Y, Zhu X, Li S, Huang Y, Qu P, Xu M. *Anal Chem*, 2018, 90: 12449–12455
26 Lei L, Geng R, Xu Z, Dang Y, Hu X, Li L, Geng P, Tian Y, Zhang W. *Anal Chem*, 2019, 91: 8129–8136
27 Wang YL, Fan C, Xin B, Zhang JP, Luo T, Chen ZQ, Zhou QY, Yu Q, Li XN, Huang ZL, Li C, Zhu MQ, Tang BZ. *Mater Chem Front*, 2018, 2: 1554–1562
28 Dou WT, Zhang JJ, Li Q, Guo Z, Zhu W, Chen GR, Zhang HY, He XP. *ChemBioChem*, 2019, 20: 1856–1860
29 Tan H, Zhou K, Yan J, Sun H, Pistolozzi M, Cui M, Zhang L. *Sens Actuat B-Chem*, 2019, 298: 126903
30 Yang Y, Li S, Zhang Q, Kuang Y, Qin A, Gao M, Li F, Tang BZ. *J Mater Chem B*, 2019, 7: 2434–2441
31 Luo J, Xie Z, Lam JWY, Cheng L, Tang BZ, Chen H, Qiu C, Kwok HS, Zhan X, Liu Y, Zhu D. *Chem Commun*, 2001, 1740–1741
32 Hong Y, Meng L, Chen S, Leung CWT, Da LT, Faisal M, Silva DA, Liu J, Lam JWY, Huang X, Tang BZ. *J Am Chem Soc*, 2012, 134: 1680–1689
33 Kumar M, Hong Y, Thorn DC, Ecroyd H, Carver JA. *Anal Chem*, 2017, 89: 9322–9329
34 Ou H, Dai S, Liu R, Ding D. *Sci China Chem*, 2019, 62: 929–932
35 Ni X, Zhang X, Duan X, Zheng HL, Xue XS, Ding D. *Nano Lett*, 2019, 19: 318–330
36 Mei J, Huang Y, Tian H. *ACS Appl Mater Interfaces*, 2018, 10: 12217–12261
37 Gao Z, Gao H, Zheng D, Xu T, Chen Y, Liang C, Wang L, Ding D, Yang Z. *Sci China Chem*, 2020, 63: 398–403
38 Li J, Gao H, Liu R, Chen C, Zeng S, Liu Q, Ding D. *Sci China Chem*, 2020, 63: 1428–1434
39 Yu CYY, Zhang W, Kwok RTK, Leung CWT, Lam JWY, Tang BZ. *J Mater Chem B*, 2016, 4: 2614–2619
40 Donabedian PL, Pham TK, Whitten DG, Chi EY. *ACS Chem Neurosci*, 2015, 6: 1526–1535
41 Rahimi F, Maiti P, Bitan G. *J Vis Exp*, 2009, 23: e1071
42 Frisch MJ, Trucks GW, Schlegel HB, Scuseria GE, Robb MA, Cheeseman JR, Scalmani G, Barone V, Mennucci B, Petersson GA, Nakatsuji H, Caricato M, Li X, Hratchian HP, Izmaylov AF, Bloino J, Zheng G, Sonnenberg JL, Hada M, Ehara M, Toyota K, Fukuda R, Hasegawa J, Ishida M, Nakajima T, Honda Y, Kitao O, Nakai H, Vreven T, Montgomery JA, Jr. Peralta JE, Ogliaro F, Bearpark M, Heyd JJ, Brothers E, Kudin KN, Staroverov VN, Kobayashi R, Normand J, Raghavachari K, Rendell A, Burant JC, Iyengar SS, Tomasi J, Cossi M, Rega N, Millam JM, Klene M, Knox JE, Cross JB, Bakken V, Adamo C, Jaramillo J, Gomperts R, Stratmann RE, Yazyev O, Austin AJ, Cammi R, Pomelli C, Ochterski JW, Martin RL, Morokuma K, Zakrzewski VG, Voth GA, Salvador P, Dannenberg JJ, Dapprich S, Daniels AD, Farkas Ö, Foresman JB, Ortiz JV, Cioslowski J, Fox DJ. Gaussian 09, Revision A02. Wallingford CT: Gaussian, Inc., 2009
43 Lührs T, Ritter C, Adrian M, Riek-Loher D, Bohrmann B, Döbeli H, Schubert D, Riek R. *Proc Natl Acad Sci USA*, 2005, 102: 17342–17347
44 Tomaselli S, Esposito V, Vangone P, van Nuland NAJ, Bonvin AMJJ, Guerrini R, Tancredi T, Temussi PA, Picone D. *ChemBioChem*, 2006, 7: 257–267
45 Protein Data Bank. A Structural View of Biology. http://www.rcsb.org/, accessed on 2021-08-10
46 Sanner MF, Huey R, Dallakyan S, Carrillo C, Chan K, Coon S, Gillet A, Karnati S, Lindstrom W, Morris MG, Norledge B, Omelchenko A, Stoffler D, Tschinke V, Vareille G, Zhao Y. MGL Tools-1.5.7. Molecular Graphics Laboratory, The Scripps Research Institute, 1999–2011
47 DeLano WL. The PyMOL molecular graphics system. Palo Alto: DeLano Scientific LLC, 2008
48 Oakley H, Cole SL, Logan S, Maus E, Shao P, Craft J, Guillozet-Bongaarts A, Ohno M, Disterhoft J, Van Eldik L, Berry R, Vassar R. *J Neurosci*, 2006, 26: 10129–10140
49 Fu H, Cui M, Zhao L, Tu P, Zhou K, Dai J, Liu B. *J Med Chem*, 2015, 58: 6972–6983
50 Liu H, Qian C, Yang T, Wang Y, Luo J, Zhang C, Wang X, Wang X, Guo Z. *Chem Sci*, 2020, 11: 7158–7169